

Fast constrained sampling in pre-trained diffusion models

Alexandros Graikos¹ Nebojsa Jojic² Dimitris Samaras¹

Abstract

Large denoising diffusion models, such as Stable Diffusion, have been trained on billions of image-caption pairs to perform text-conditioned image generation. As a byproduct of this training, these models have acquired general knowledge about image statistics, which can be useful for other inference tasks. However, when confronted with sampling an image under new constraints, e.g. generating the missing parts of an image, using large pre-trained text-to-image diffusion models is inefficient and often unreliable. Previous approaches either utilize backpropagation, making them significantly slower and more memory-demanding than text-to-image inference, or only enforce the constraint locally, failing to capture critical long-range correlations. In this work, we propose an algorithm that enables fast and high-quality generation under arbitrary constraints. We observe that, during inference, we can interchange between gradient updates computed on the noisy image and updates computed on the final, clean image. This allows us to employ a numerical approximation to expensive gradient computations, incurring significant speed-ups in inference. Our approach produces results that rival or surpass the state-of-the-art training-free inference approaches while requiring a fraction of the time. We demonstrate the effectiveness of our algorithm under both linear and non-linear constraints. An implementation is provided [at this link](#).

1. Introduction

The development of large text-to-image models (Nichol et al., 2022; Rombach et al., 2022; Ramesh et al., 2022; Saharia et al., 2022b) has made denoising diffusion (Sohl-Dickstein et al., 2015; Ho et al., 2020) the go-to approach for capturing complex data distributions in high-dimensional

spaces, such as images. By training on billions of text-image pairs, these models have acquired general knowledge about the image space, beyond text-to-image generation. This knowledge has been useful in quickly adapting to new conditions (Zhang et al., 2023) as well as utilizing model features to solve downstream image tasks (Tang et al., 2023).

The simplest way to utilize this knowledge is by fine-tuning the model. However, fine-tuning may require non-trivial computational resources and thus, previous works have focused on developing algorithms for conditional generation using *only* the pre-trained model (Chung et al., 2023; Rout et al., 2023; Chung et al., 2024; Yu et al., 2023; He et al., 2024). These methods modify the diffusion sampling process by computing additional gradient terms that move the sample towards the condition while denoising. When these gradients are computed using backpropagation through the model weights, there is a significant increase in inference time. On the other hand, when attempting to save computation by not propagating the condition information through the model, the generated image fails to capture the necessary long-range correlations.

As an example, in Figure 1, we use different algorithms to fill in the missing half of an image. Methods that backpropagate through the denoiser model (LDPS, PSLD (Rout et al., 2023), FreeDoM (Yu et al., 2023)) require significantly more time to run and do not consistently produce realistic results. Algorithms that do not compute gradients through the denoiser (MPGD (He et al., 2024)) fail to propagate the condition to distant pixels.

With the shortcomings of existing approaches in mind, we pose the following question: Can we avoid backpropagation through the model weights while at the same time maintaining long-range consistency when updating the sample with the conditioning signal? We observe that when a constraint increases the intensity of pixels in the predicted clean image, these pixel values are also expected to increase in the noisy image. From the diffusion point of view, the diffusion latent x_{t-1} is a linear combination of the current noisy image x_t and the predicted final image \hat{x}_0 (Song et al., 2020), therefore any change in x_t can be also performed by changes in \hat{x}_0 .

This observation tells us that changes computed in the noisy and clean images can be interchanged. We find that this

¹Stony Brook University, Stony Brook, NY ²Microsoft Research, Redmond, WA. Correspondence to: Alexandros Graikos <agraikos@cs.stonybrook.edu>.



Figure 1. When tasked with completing the missing half of an image, previous methods are slow and fail to capture the important long-range dependencies between image pixels. The proposed algorithm generates a plausible image at a fraction of the time.

can be exploited to devise a new training-free conditional sampling algorithm that employs a numerical approximation for the expensive gradient computations. This allows us to speed up inference time while maintaining long-range dependencies in the image (Figure 1). We take inspiration from Newton’s method and pose the proposed algorithm as an approximation to Newton steps that avoids computing the Jacobian inverse by using the Jacobian matrix directly.

We test the effectiveness of our proposed approach by generating images under both linear and non-linear constraints. We first show that our approach matches the results of state-of-the-art methods on free-form inpainting and $8\times$ super-resolution at a fraction of the inference time. We then demonstrate how existing methods fail at inpainting large regions (25% of the image), while our algorithm obtains results closer to explicitly fine-tuning the diffusion model on inpainting. Finally, we apply our algorithm on non-linear constraints to perform style-guided and mask-guided generation, where we show that the proposed method synthesizes images that satisfy the constraints better than existing approaches.

2. Background

2.1. Denoising Diffusion Models

Denoising diffusion models, proposed for image generation by Ho et al. (2020), have now been widely adopted mainly due to their exceptional ability to synthesize diverse and high-quality samples. The original formulation views the training and inference process as a hierarchical latent variable model $\mathbf{x}_T \rightarrow \mathbf{x}_{T-1} \rightarrow \dots \rightarrow \mathbf{x}_1 \rightarrow \mathbf{x}_0$, where the final latent is distributed normally $\mathbf{x}_T \sim N(\mathbf{0}, \mathbf{I})$ and $p(\mathbf{x}_0)$ represents the data distribution. After choosing a noise schedule a_t that defines the *forward* transitions $\mathbf{x}_t \rightarrow \mathbf{x}_{t+1}$ that corrupt the data with Gaussian noise, usually centered at $\sqrt{\frac{a_{t+1}}{a_t}}\mathbf{x}_t$ and with variance $(1 - \frac{a_{t+1}}{a_t})$, the model is trained to reverse each individual step in the diffusion process by predicting the noise added to the clean sample. In this formulation, the predicted noise is shown to approximate the score function $\nabla_{\mathbf{x}_t} \log p_t(\mathbf{x}_t)$ (Song et al., 2021)

of the diffusion latent variables.

Further iterations of denoising diffusion introduced classifier guidance (Dhariwal & Nichol, 2021), which adapted a pre-trained unconditional diffusion model for conditional sampling by training an additional classifier $p(\mathbf{y}|\mathbf{x}_t)$. During inference, each reverse step is also perturbed by the gradient $\nabla_{\mathbf{x}_t} \log p(\mathbf{y}|\mathbf{x}_t)$ which guides the diffusion latent \mathbf{x}_t towards regions that also satisfy the condition \mathbf{y} . Classifier-free guidance (Ho & Salimans, 2022) eliminated the need for training an additional classifier to perform conditional generation by incorporating it into the base diffusion model training process.

Latent diffusion models (LDMs) proposed Rombach et al. (2022), reduced the complexity of training large diffusion models by training the diffusion in the latent space of a pre-trained autoencoder. By utilizing an encoder \mathcal{E} and decoder \mathcal{D} that accurately reconstruct images $\mathbf{x}_0 \approx \mathcal{D}(\mathcal{E}(\mathbf{x}_0))$, the diffusion process can be made more efficient as the learned redundant information in an image is left for the decoder to reconstruct. Most large text-to-image diffusion models, such as Stable Diffusion (Podell et al., 2024), are based on this encoder-decoder approach to reduce complexity.

2.2. Gradient descent steps for constrained sampling

Previous works have studied whether large pre-trained diffusion models, which required significant investment to train, can be directly used for inference under novel conditions without additional tuning for each different constraint (Chung et al., 2023). The most typical problem formulation is denoising the sequence $\mathbf{x}_T, \mathbf{x}_{T-1}, \dots, \mathbf{x}_1, \mathbf{x}_0$ under the linear constraint on the final signal in the form $\mathbf{A}\mathbf{x}_0 = \mathbf{y}$, or using a relaxed version that requires minimization of $\|\mathbf{A}\mathbf{x}_0 - \mathbf{y}\|_2^2$, possibly as part of the likelihood function $p(\mathbf{y}|\mathbf{x}_0) = \mathcal{N}(\mathbf{y}; \mathbf{A}\mathbf{x}_0, \sigma^2 \mathbf{I})$.

In contrast to classifier guidance, which explicitly trained a separate model for the likelihood $p(\mathbf{y} | \mathbf{x}_t)$, the linear constraint only applies to the final, noise-free image \mathbf{x}_0 . Thus, existing methods rely on Tweedie’s formula (Efron, 2011), by which denoising diffusion models approximating

$\nabla_{\mathbf{x}_t} \log p_t(\mathbf{x}_t)$ can be used to express the expected value of \mathbf{x}_0 , denoted as $\hat{\mathbf{x}}_0$. Including the constraint as if an additional observed variable \mathbf{y} was generated requires the addition of the term $\nabla_{\mathbf{x}_t} \log p(\mathbf{y} | \mathbf{x}_t)$ to every diffusion sampling step, and most previous methods focused on different approximations of $p(\mathbf{y} | \mathbf{x}_t)$ using the estimated $\hat{\mathbf{x}}_0$.

Regardless of how the constraint gradient is applied, the regular denoising diffusion steps are altered so that at each t , the generated latent \mathbf{x}_t is moved in the direction reducing the cost

$$C(\mathbf{x}_t) = (\mathbf{A}\hat{\mathbf{x}}_0(\mathbf{x}_t) - \mathbf{y})^T (\mathbf{A}\hat{\mathbf{x}}_0(\mathbf{x}_t) - \mathbf{y}). \quad (1)$$

For example, in the case of inpainting missing pixels, the matrix \mathbf{A} extracts the subsection of the known pixels in image \mathbf{x}_0 to be compared with a given target \mathbf{y} . The estimated expected value of \mathbf{x}_0 at the end of the chain is provided by the diffusion model as a nonlinear function $\hat{\mathbf{x}}_0(\mathbf{x}_t)$ learned by the denoiser network during training. Typically, these moves are gradient descent moves, i.e. moves of \mathbf{x}_t in the direction of $-\mathbf{e}_t$ where

$$-\mathbf{e}_t = -\nabla_{\mathbf{x}_t} C(\mathbf{x}_t) = -\mathbf{J}^T \mathbf{A}^T (\mathbf{A}\hat{\mathbf{x}}_0 - \mathbf{y}) = -\mathbf{J}^T \mathbf{e}, \quad (2)$$

$$\mathbf{J} = \nabla_{\mathbf{x}_t} \hat{\mathbf{x}}_0(\mathbf{x}_t), \quad \mathbf{e} = \mathbf{A}^T (\mathbf{A}\hat{\mathbf{x}}_0 - \mathbf{y}). \quad (3)$$

Note that we name the error signal \mathbf{e} as the (negative) direction of the gradient w.r.t. \mathbf{x}_0 itself, and the \mathbf{e}_t is the matching move in \mathbf{x}_t .

The matrix \mathbf{A}^T inverses the operation of \mathbf{A} and can usually be computed for each task a-priori. However, computation of the full Jacobian \mathbf{J} is impractical, so the gradient is instead computed using backpropagation through $C(\mathbf{x}_t)$. In (Chung et al., 2023) and (Chung et al., 2024) for example, gradient steps of this form are applied to \mathbf{x}_t at each step t of generation before moving on to the next stage. As optimization of \mathbf{x}_t might reduce the total noise in the image below what the denoising at $t-1$ was trained for, the gradient steps moving \mathbf{x}_t towards optimizing $C(\mathbf{x}_t)$ can be combined with adding additional noise, which could also be seen as a form of stochastic averaging, as done by Yu et al. (2023).

3. Method

3.1. Approximate Newton steps

We start by observing that a Newton optimization step, instead of moving \mathbf{x}_t in the gradient descent direction $\mathbf{J}^T \mathbf{e}$, moves it in the direction $\mathbf{J}^{-1} \mathbf{e}$. We demonstrate that on a more general form of the cost

$$C(\mathbf{x}_t) = (f(\hat{\mathbf{x}}_0(\mathbf{x}_t)) - \mathbf{y})^T (f(\hat{\mathbf{x}}_0(\mathbf{x}_t)) - \mathbf{y}), \quad (4)$$

for some target \mathbf{y} to be matched with projection function f , which in the linear case is $f(\mathbf{x}) = \mathbf{A}\mathbf{x}$. The Gauss-Newton

optimization would first approximate

$$f(\hat{\mathbf{x}}_0(\mathbf{x}_t - \mathbf{e}_t)) \approx f(\hat{\mathbf{x}}_0(\mathbf{x}_t)) - \mathbf{J}_f \mathbf{J} \mathbf{e}_t, \quad (5)$$

where \mathbf{J}_f is the Jacobian of f . We then rewrite the cost of move $-\mathbf{e}_t$ as

$$C(\mathbf{x}_t - \mathbf{e}_t) = (f(\hat{\mathbf{x}}_0(\mathbf{x}_t)) - \mathbf{J}_f \mathbf{J} \mathbf{e}_t - \mathbf{y})^T (f(\hat{\mathbf{x}}_0(\mathbf{x}_t)) - \mathbf{J}_f \mathbf{J} \mathbf{e}_t - \mathbf{y}). \quad (6)$$

The cost is minimized by setting $\nabla_{\mathbf{e}_t} C = 0$ to get the system

$$\mathbf{J}^T \mathbf{J}_f^T (f(\hat{\mathbf{x}}_0(\mathbf{x}_t)) - \mathbf{y}) = \mathbf{J}^T \mathbf{J}_f^T \mathbf{J}_f \mathbf{J} \mathbf{e}_t \\ \Leftrightarrow \mathbf{e}_t = \mathbf{J}^{-1} \mathbf{J}_f^{-1} (f(\hat{\mathbf{x}}_0(\mathbf{x}_t)) - \mathbf{y}) \quad (7)$$

$$\mathbf{e}_t = \mathbf{J}^{-1} \mathbf{e}, \quad \mathbf{e} = \mathbf{J}_f^{-1} (f(\hat{\mathbf{x}}_0(\mathbf{x}_t)) - \mathbf{y}), \quad (8)$$

assuming the inverses exist. In the case of $f(\mathbf{x}) = \mathbf{A}\mathbf{x}$ for inpainting and superresolution tasks, where \mathbf{y} is lower-dimensional, the inverse of \mathbf{J}_f , obviously is not defined, but we can use the pseudoinverse. Similarly, for a non-linear f , we can compute \mathbf{e} using numerical methods, e.g. backpropagation through f when it is a neural network.

Therefore, \mathbf{e} is the same in both gradient descent and Newton optimization, but the relationship to \mathbf{e}_t is different:

$$\text{GD} : \mathbf{e}_t = \mathbf{J}^T \mathbf{e}, \quad \text{Newton} : \mathbf{J} \mathbf{e}_t = \mathbf{e} \quad (9)$$

The gradient descent step can be computed without directly evaluating the Jacobian by back-propagation on the scalar cost C . For the computation of $\mathbf{J}^{-1} \mathbf{e}$ on the other hand, we have no such method. However, we can efficiently compute the move

$$\epsilon \mathbf{e}_t = \epsilon \mathbf{J} \mathbf{e}. \quad (10)$$

We follow the Newton recipe suggesting multiplication of the error by \mathbf{J} in Eq. (9) but multiply \mathbf{e} by it instead of \mathbf{e}_t . Intuitively, this is justified by the fact that the mode of \mathbf{x}_{t-1} in the next stage of denoising is a weighted sum of $\hat{\mathbf{x}}_0$ and \mathbf{x}_t , meaning that the changes in \mathbf{x}_t can be equivalently represented by proportional moves in the same direction of either component. This is the consequence of the modeling assumption that in the posterior the stages are separated by independent Gaussian noise, and early inpainting models simply assumed $\mathbf{e}_t = \mathbf{e}$, missing on the effect of the image prior $p(\mathbf{x}_0)$, which is implicit in the learned function $\mathbf{x}_0(\mathbf{x}_t)$. In addition to that, in Appendix A.1 we provide an analysis of the convergence on the algorithm using *inexact Newton methods* (Dembo et al., 1982).

The direction of optimization we propose in Eq. (10) has at least two advantages over the usual gradient descent update. First, the direction $\epsilon \mathbf{e}_t$ can be computed numerically to save both on computation (2-fold) and memory (2.5-fold) compared to using backpropagation on the cost in Eq. (1).

To derive that update, consider the function $f(s) = \hat{x}_0(\mathbf{x}_t - se)$ where the variable s is scalar. Its derivative at $s = 0$ is

$$\frac{df}{ds} = -\mathbf{J}e, \quad (11)$$

and so the direction \mathbf{h} can be approximated numerically using the approximate derivative of $f(s)$ at $s = 0$

$$f' = \frac{1}{\delta} [\hat{x}_0(\mathbf{x}_t + \delta \mathbf{e}) - \hat{x}_0(\mathbf{x}_t)], \quad (12)$$

$$\mathbf{e}_t = -\epsilon \mathbf{J}e \approx \frac{\epsilon}{\delta} [\hat{x}_0(\mathbf{x}_t + \delta \mathbf{e}) - \hat{x}_0(\mathbf{x}_t)], \quad (13)$$

requiring no backpropagation but instead two forward passes through the network: one to compute $\hat{x}_0(\mathbf{x}_t)$ and another to compute \hat{x}_0 for the \mathbf{x}_t perturbed in the negative direction of the error vector.

The second advantage comes from the asymmetry of the Jacobian \mathbf{J} . The theoretically optimal $\mathbf{x}_0(\mathbf{x}_t)$ would have a symmetric Jacobian, as \hat{x}_0 approximates the true expectation $E[\mathbf{x}_0|\mathbf{x}_t] = \frac{1}{\sqrt{\alpha_t}}[\mathbf{x}_t + \mathbf{v}_t \nabla_{\mathbf{x}_t} \log p_t(\mathbf{x}_t)]$, and the gradient of this is indeed symmetric:

$$\nabla_{\mathbf{x}_t} E[\mathbf{x}_0|\mathbf{x}_t] = \frac{1}{\sqrt{\alpha_t}} [\mathbf{I} + \mathbf{v}_t \nabla^2 \log p_t(\mathbf{x}_t)]. \quad (14)$$

This would render the gradient descent and the proposed update equivalent. In Section 3.2, we show that in practice, the trained denoiser models do not satisfy this ideal condition, making the two update directions noticeably different. Whether the denoising diffusion models are trained with score matching in mind (Song et al., 2021) or using the variational method of Ho et al. (2020), they do not directly optimize to match the real score $\nabla_{\mathbf{x}_t} \log p_t(\mathbf{x}_t)$ everywhere nor are they constrained to produce symmetric Jacobians. We hypothesize that this discrepancy in the two update directions is one of the reasons why our optimization of \mathbf{x}_t may be more suitable for some applications, as demonstrated in Section 4.

Lastly, the proposed update of Eq. (10) only requires us to provide the direction of the error \mathbf{e} , which points locally towards a lower cost for our constraint on \mathbf{x}_0 . As already discussed, for linear constraints such as inpainting, this direction can be obtained in closed form using the inverse of the operator expressed by \mathbf{A} . For non-linear constraints, such as style-guidance, \mathbf{e} can be computed using backpropagation through the differentiable non-linear constraint model. Note that this backpropagation operation does not backpropagate through the denoiser itself, but only through the constraint w.r.t. the estimated \hat{x}_0 . A general version of the proposed algorithm for linear and non-linear constraints is presented in Algorithm 1. We choose DDIM as our sampling algorithm (Song et al., 2020). Applying other sampling methods should be intuitive by interleaving the diffusion and our gradient updates on \mathbf{x}_t .

Algorithm 1 The proposed algorithm for constrained sampling using a pre-trained diffusion model.

```

1: Input: Pre-trained diffusion model  $\hat{x}_0(\mathbf{x}_t)$ , constraint
    $C(\mathbf{x}_0, \mathbf{y}) = \|f(\hat{x}_0(\mathbf{x}_t)) - \mathbf{y}\|_2^2$ , condition  $\mathbf{y}$ , gradient
   step size  $\delta$ , iterations  $K$ , learning rate  $\lambda$ , diffusion step
   size  $s$  and schedule parameters  $\alpha_i, \beta_i$ 
2:  $\mathbf{x}_T \sim N(\mathbf{0}, \mathbf{I})$ 
3: for  $t \in \{T, T-s, T-2s, \dots, s\}$  do
4:   for  $i \in \{1, 2, \dots, K\}$  do
5:      $\mathbf{e} = \mathbf{J}_f^{-1}(f(\hat{x}_0(\mathbf{x}_t)) - \mathbf{y})$  {Task-dependent}
6:      $\mathbf{e}_t = [\hat{x}_0(\mathbf{x}_t + \delta \mathbf{e}) - \hat{x}_0(\mathbf{x}_t)]/\delta$ 
7:      $\mathbf{x}_t = \mathbf{x}_t + \lambda \mathbf{e}_t$ 
8:   end for
9:    $\mathbf{z}_t \sim N(\mathbf{0}, \mathbf{I})$ 
10:   $\epsilon_t = \frac{1}{\sqrt{1-\alpha_{t-s}}} \mathbf{x}_t - \frac{\sqrt{\alpha_{t-s}}}{\sqrt{1-\alpha_{t-s}}} \hat{x}_0(\mathbf{x}_t)$ 
11:   $\mathbf{x}_{t-s} = \sqrt{\alpha_{t-s}} \hat{x}_0(\mathbf{x}_t) + \sqrt{1-\alpha_{t-s}} \epsilon_t + \beta_{t-s} \mathbf{z}_t$ 
12: end for
13: Return:  $\mathbf{x}_0$ 

```

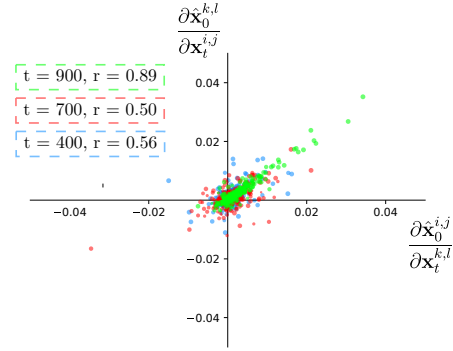


Figure 2. Sample pairs $(i, j), (k, l)$ of the denoiser Jacobian $\nabla_{\mathbf{x}_t} \hat{x}_0 = \nabla_{\mathbf{x}_t} E[\mathbf{x}_0|\mathbf{x}_t]$ for different timesteps t . We observe that the Jacobian is not symmetric, justifying the difference between the proposed update steps and the previously used gradient descent steps.

3.2. Symmetry of the Jacobian and difference in updates

Although, theoretically, the Jacobian of the denoiser should be symmetric (Eq. 14), the trained diffusion model does not exactly match the real score and can yield non-symmetric Jacobians. In Figure 2, we verify this claim with a simple experiment; we select a random image from the ImageNet (Deng et al., 2009) validation set and employ the Stable Diffusion 1.5 model (Podell et al., 2024) to denoise at three different noise levels $t = \{900, 700, 400\}$. We encode the image using the VAE encoder, scale it and add appropriate noise to get the intermediate diffusion latent for each timestep. We then give the noisy image to the denoiser network and compute the gradients $\partial \hat{x}_0^{k,l} / \partial x_t^{i,j}$ and $\partial \hat{x}_0^{i,j} / \partial x_t^{k,l}$ for randomly chosen pixels $(i, j), (k, l)$ using backpropagation. When we plot the gradients and com-

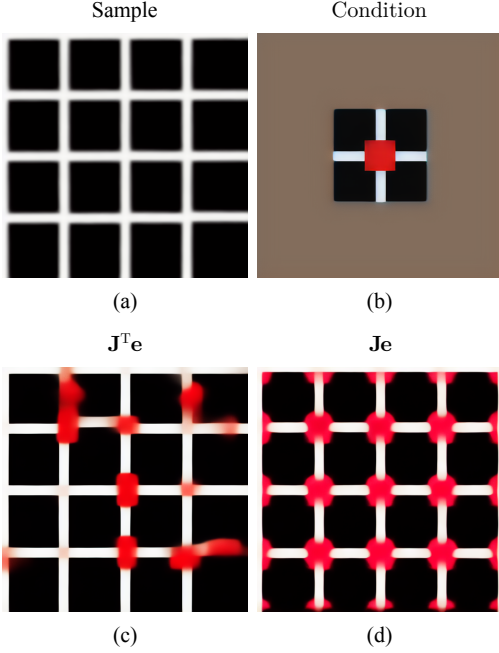


Figure 3. We present a simple experiment to compare the proposed gradient update $\mathbf{J}e$ with that of previous methods $\mathbf{J}^T e$. The goal is to update a noisy version of the image shown in (a) at $t = 800$, such that the diffusion model’s prediction of the final image includes a red square in the middle, shown in (b). The results of gradient descent in (c) and our gradient update in (d) demonstrate that updates performed by previous methods lead to a considerably different result than the update we propose in this paper.

pute the correlation coefficient r we observe that the values deviate from $y = x$, which would indicate a symmetric Jacobian.

Having shown that the Jacobian is not symmetric, we expect to find differences between the gradient updates of gradient descent (Eq. 3) and our proposed update (Eq. 10). To highlight these differences, we set up a toy experiment where we update an identical initial image with the two different directions, under the same condition. The experiment is showcased in Figure 3 and again utilizes the Stable Diffusion 1.5 model. We create a synthetic black-and-white grid image (Figure 3 (a)), which we blur, deterministically encode, scale and noise to get a diffusion latent at $t = 800$. We then set up a constraint where we add a red square to the center of the original image (Figure 3 (b)). The brown region in the constraint indicates masked-out values, or equivalently, where we will not be applying a constraint. Instead of decoding the image and applying the constraint in image space, we also encode the constraint image and apply it directly in the Stable Diffusion latent space.

We run 5 gradient updates with the same learning rate of 1 for each and demonstrate the final predicted \hat{x}_0 for the

$\mathbf{J}^T e$ update of (3) (Figure 3 (c)) and the proposed $\mathbf{J}e$ (10) (Figure 3 (d)). The final result shows how the model intends to change the *entire* image when asked to add a red square in the middle. We find that the resulting images differ substantially, with the proposed direction producing a more coherent image that tries to copy the newly introduced texture to the correct locations, i.e. the intersections of the lines. Although this is an empirical observation, we hypothesize that the two different directions can have vastly different effects on the image. In the Appendix A.2, we further visualize differences between $\mathbf{J}^T e$ and $\mathbf{J}e$, and in C.5, we repeat the previous experiment over multiple seeds.

4. Experiments

4.1. Linear Constraints

We first verify our algorithm by generating images under linear constraints, which has been the main application of many previous algorithms (Chung et al., 2023; Rout et al., 2023; Chung et al., 2024). We follow the evaluation setting of Saharia et al. (2022a) and test our method on ImageNet (Deng et al., 2009), using the first 1000 images from the 10k validation set of the `ctest10k` split. As our evaluation metrics, we measure the PSNR and LPIPS (Zhang et al., 2018) between the generated and real images, as well as the FID (Heusel et al., 2017) between the real and generated sets. We use Stable Diffusion 1.4, which is pre-trained on the LAION (Schuhmann et al., 2022) text-image pair dataset. All experiments were run on NVIDIA RTX A5000 24GB GPUs.

Free-form Inpainting & Super-resolution We follow the previously described experiment settings of free-form inpainting and $8\times$ super-resolution. For free-form inpainting, the masks are randomly sampled and mask out 10-20% of the image pixels, as done by Saharia et al. (2022a). For inpainting with our method, we opt to directly operate on the Stable Diffusion latent given that Stable Diffusion VAE mostly compresses information locally. We apply the masking in pixel space, encode the masked image and inpaint with the unmasked VAE latents. We also apply a 3×3 dilation kernel on the pixel mask before downsampling, masking out some extra pixels along the edge that we find the VAE fails to encode. For inpainting, we set the number of optimization steps $K = 5$ over which we linearly decrease the learning rate λ from 0.5 to 0.1. For super-resolution, we use $K = 10$ and a constant $\lambda = 0.1$. We perform only 20 DDIM (Song et al., 2020) steps for all experiments.

Regarding super-resolution, we cannot apply the constraint in the VAE latent space as image pixel downsampling does not correspond to downsampling VAE latents. To compute the error direction e we backpropagate the pixel-level constraint cost $(\mathcal{A}\mathcal{D}(x_t) - y)^T(\mathcal{A}\mathcal{D}(x_t) - y)$ through the



Figure 4. Comparison between our method and existing algorithms on free-form inpainting and $8\times$ super-resolution. We directly use the images and results from (Chung et al., 2024) since there is no code available to replicate their method.

Method	Inpaint (Free-form)			SR ($\times 8$)			
	PSNR \uparrow	LPIPS \downarrow	FID \downarrow	PSNR \uparrow	LPIPS \downarrow	FID \downarrow	Time
P2L (Chung et al., 2024)	21.99	0.229	32.82	23.38	0.386	51.81	30min*
LDPS	21.54	0.332	46.72	23.21	0.475	61.09	6min
PSLD (Rout et al., 2023)	20.92	0.251	40.57	23.17	0.471	60.81	8min
Ours	21.73	0.258	19.39	24.26	0.455	60.99	15s/1min

Table 1. Quantitative evaluation (PSNR, LPIPS, FID) on free-form inpainting and $8\times$ superresolution on ImageNet. Our algorithm is competitive with the results of P2L which requires at least $30\times$ more time for a single sample.

decoder network and utilize the resulting gradient w.r.t. the latent as the error direction. We note that by setting $e = -\partial C(\mathcal{D}(\mathbf{x}_t))/\partial \mathbf{x}_t$ we only require backpropagation through the decoder model, which is significantly less expensive than backpropagating through the denoiser network, as done by previous works. For both degradations, we also include additive white Gaussian noise with $\sigma_y = 0.05$.

We present the results on free-form inpainting and $8\times$ super-resolution (SR) in Table 1. In inpainting, we find that our method generates better-aligned parts for the missing image regions, reflected in the significant improvement in FID, while obtaining similar PSNR and LPIPS scores to state-of-the-art methods. For super-resolution, although the improvements are smaller, we still find that we can compete with existing methods in both the quality and faithfulness of the generated images.

The main advantage we showcase is inference time; our approach achieves similar or better results to every other existing method while only requiring a fraction of the computation. When we do not perform backpropagation through the VAE decoder (inpainting), our method requires only 15 seconds. In super-resolution, where we perform more optimization steps and backpropagate, the time increases to 1 minute. In contrast, P2L (Chung et al., 2024), the best-performing method, requires 30 minutes per single image since it relies on additional backpropagation steps through

the denoiser to infer the text condition. Since there is no publicly available implementation for P2L we report the results directly from the paper and estimate the inference time as $5\times$ that of LDPS (Chung et al., 2023), which the authors mentioned as a reasonable expectation as it linearly scales with the number of text prompt optimization iterations.

Box Inpainting In the previous experiments, we observed that our method performed better in inpainting, which required the model to infer more missing information in the given image than in super-resolution. We further push the model by asking it to inpaint a box that covers 25% of the input image. In the comparisons we also include FreeDoM (Yu et al., 2023), which, although not previously shown on inpainting, claims to be a fast training-free inference approach for any condition. We also include the fine-tuned SD-Inpaint model (Rombach et al., 2022), which required 500k additional training steps.

We present the results on box inpainting in Table 2 and Figure 5. Our approach outperforms all existing training-free methods in all metrics and is the closest to the fine-tuned SD-Inpaint model, which we consider an upper limit. Qualitatively, we find that LDPS and PSLD, which perform a lot of denoising steps, generate blurry parts that align with the average appearance over the rest of the image. FreeDoM, the faster baseline, although generating non-blurry

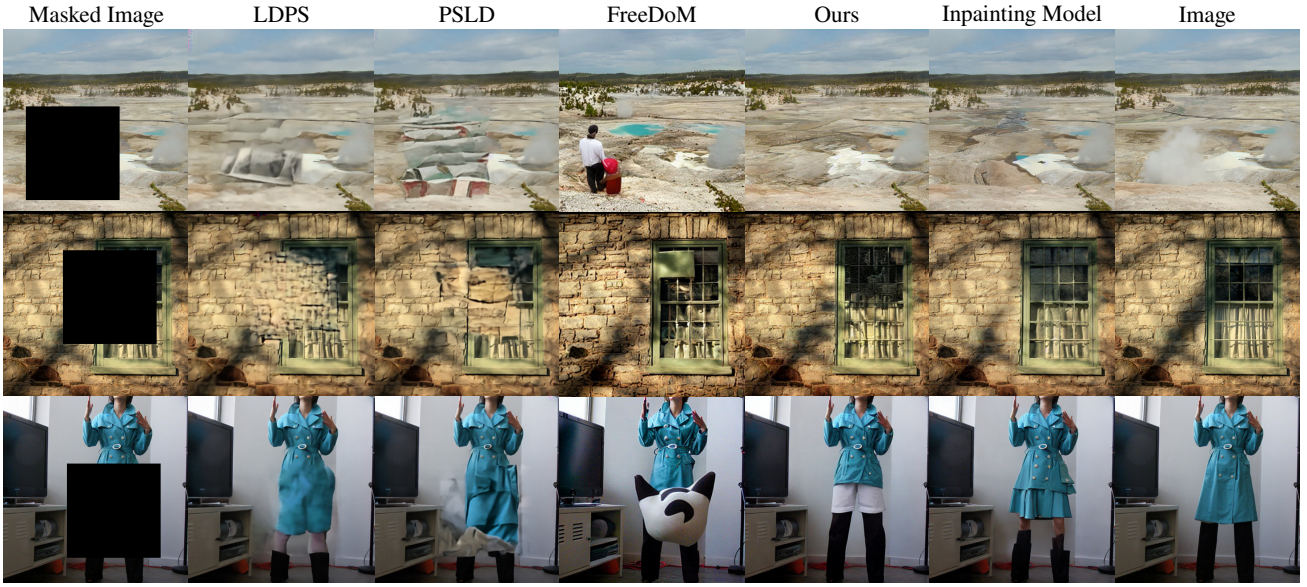


Figure 5. Qualitative evaluation of large area (box) inpainting on ImageNet. Our method provides results close to the fine-tuned inpainting model while requiring a fraction of the time to run per image.

Method	Inpaint (Box)			Time
	PSNR \uparrow	LPIPS \downarrow	FID \downarrow	
LDPS	17.52	0.42	76.32	6min
PSLD	17.30	0.38	74.02	8min
FreeDoM	16.18	0.42	55.68	1min
(Yu et al., 2023)				
Ours	18.30	0.30	42.01	15s
SD-Inpaint	19.05	0.28	32.93	4s

Table 2. Quantitative evaluation (PSNR, LPIPS, FID) on large area (box) inpainting.

parts, frequently fails to maintain consistency with the rest of the image. Our method achieves both high quality and consistency in a shorter time as all previous methods back-propagate through the denoiser weights. In Appendix C.1 we ablate the steps K and learning rate λ hyperparameters.

4.2. Style-guided generation

Our algorithm can be applied to non-linear differentiable constraints using backpropagation to approximate e . Computing this gradient direction does not require backpropagation through the denoiser but through the separate, more lightweight ‘critic’ network f . We demonstrate this with the non-linear constraint of style-guided generation.

The goal is to generate an image that simultaneously follows the style of a reference image x_{ref} and a given text prompt. Following previous works (Yu et al., 2023; He et al., 2024) which also perform style-guided generation, we do this by

matching the statistics of CLIP (Radford et al., 2021) features between the reference and the generated images. We minimize the Frobenius norm between the Gram matrices (Gatys et al., 2016) of the 2nd layer CLIP features, making the cost to be minimized

$$\|\text{Gram}(\text{CLIP}_2(x_{ref})) - \text{Gram}(\text{CLIP}_2(\hat{x}_0))\|_F^2. \quad (15)$$

Adhering to the evaluation of Yu et al (2023), we use 1000 random pairs of reference style images from WikiArt (Tan et al., 2019) and prompts from PartiPrompts (Yu et al., 2022). We measure the CLIP similarity between the generated images and the text prompts to evaluate the faithfulness to the text condition, and the final difference between the Gram matrices to evaluate the faithfulness to the style reference (Style Score). We use the CLIP ViT-B/16 model for guiding the style of the image and evaluating. We also repeat the experiment using the OpenCLIP ViT-B/32 model (Cherti et al., 2023) for guidance. We perform $K = 5$ gradient updates for every denoising step, using a linearly decreasing learning rate λ from 0.5 to 0.1 and classifier-free guidance (Ho & Salimans, 2022) $w = 2$ and $w = 5$ for the denoiser.

The results are presented in Table 3 and Figure 6. We find that our method achieves the overall best style score. Our approach is the best at minimizing the constraint which is also the the evaluation metric. Although in general, the lower the style score the more difficult it is to maintain high CLIP similarity with the prompt, we observe that our method still balances between the style and text, especially when we increase the guidance weight. We also used an OpenCLIP model to guide the style. With a CLIP model



Figure 6. Style-guided generation. We show the results of guiding Stable Diffusion with a CLIP and an OpenCLIP model, using classifier-free guidance $w = 5$. The images generated by our algorithm follow the reference style better than previous algorithms.

still as the evaluator, we achieve better style scores than the baselines that optimized directly with CLIP. Our proposed update reduces the target cost better without generating adversarial artifacts that trick the CLIP evaluation.

Regarding inference time, our method is the fastest out of all baselines, excluding the non-style-guided DDIM. The baseline of MPGD (He et al., 2024), which is comparable in inference speed, does not backpropagate the style loss through the denoiser network, but only modifies the \hat{x}_0 estimation at every denoising step. As we demonstrate in the supplementary, MPGD completely fails to propagate the constraint to distant pixels when the conditioning affects a specific region in the image. This makes it unusable in some constrained sampling settings, such as box inpainting.

4.3. Mask-guided generation

As an additional non-linear constraint, we guide the Stable Diffusion model with a separately trained face segmentation network. We employ an off-the-shelf model from [huggingface](#) and set the constraint C to be the KL divergence

Method	Style Score* ↓	CLIP ↑	Time
DDIM	761.0	31.61	9s
FreeDoM	498.8	30.14	80s
MPGD (He et al., 2024)	441.0	26.61	50s
Ours (w=2)	368.37	23.95	45s
Ours (w=5)	310.96	24.57	45s
Ours (OpenCLIP, w=5)	434.45	25.94	45s

Table 3. Quantitative evaluation of style generation. *The Style Score is what the gradient is optimizing.

between the per-pixel segmentation classes predicted for a reference image and the generated image. Using 100 images from the FFHQ (Karras et al., 2019) validation set, we run both our method and the MPGD (He et al., 2024) baseline. We chose MPGD because as the fastest baseline that works very well with 'dense' constraints, i.e. constraints that are applied to all pixels.

The results in Table 4 show that with a similar compute budget, our method achieves both faithfulness (mIoU between generated and reference images) and image quality (CLIP-FID). We used CLIP-FID because it performs better than Inception-FID on a small set of images (Kynkäänniemi et al., 2023). MPGD with a high weight (ρ) 'burns in' the segmentation mask, leading to non-realistic images, whereas a lower weight does not produce images faithful to the mask. We provide qualitative examples of the generated images and the masks used in the Appendix C.5.

Method	mIoU ↑	CLIP-FID ↓	Time
DDIM	0.09	48.78	3s
MPGD ($\rho = 1$)	0.47	77.11	1min
MPGD ($\rho = 0.5$)	0.36	56.38	1min
Ours	0.42	59.79	1min

Table 4. Mask-conditioned generation using 100 FFHQ validation set images as reference, using Stable Diffusion with the prompt 'a headshot photo'.

5. Conclusion

In this work, we presented a new algorithm for fast inference in pre-trained diffusion models under constraints. Our approach exploits the relationship between the noisy and clean images during the denoising process to perform a gradient update that requires no expensive backpropagation operations through the diffusion model. Our method produces results comparable to the state-of-the-art with a fraction of the inference time. Our approach offers a practical method to sample from large pre-trained generative image models under any condition and has the potential to enable training-free downstream applications that rely on utilizing a strong image prior.

Impact Statement

This paper presents work whose goal is to advance the field of Machine Learning. We acknowledge that there are many potential societal consequences of our work. Beyond the positives, we highlight the ability to edit images with the intent to deceive and mislead as requiring careful consideration.

Acknowledgments

Part of this work was done during an internship at Microsoft Research, Redmond. This research was also partially supported by NSF grants IIS-2123920, IIS-2212046.

References

- Arnoldi, W. E. The principle of minimized iterations in the solution of the matrix eigenvalue problem. *Quarterly of applied mathematics*, 9(1):17–29, 1951.
- Cherti, M., Beaumont, R., Wightman, R., Wortsman, M., Ilharco, G., Gordon, C., Schuhmann, C., Schmidt, L., and Jitsev, J. Reproducible scaling laws for contrastive language-image learning. In *Proceedings of the IEEE/CVF Conference on Computer Vision and Pattern Recognition*, pp. 2818–2829, 2023.
- Chung, H., Kim, J., McCann, M. T., Klasky, M. L., and Ye, J. C. Diffusion posterior sampling for general noisy inverse problems. In *The Eleventh International Conference on Learning Representations*, 2023. URL <https://openreview.net/forum?id=OnD9zGAGT0k>.
- Chung, H., Ye, J. C., Milanfar, P., and Delbracio, M. Prompt-tuning latent diffusion models for inverse problems. In *Proceedings of the 41st International Conference on Machine Learning*, volume 235 of *Proceedings of Machine Learning Research*, pp. 8941–8967. PMLR, 2024. URL <https://proceedings.mlr.press/v235/chung24b.html>.
- Dembo, R. S., Eisenstat, S. C., and Steihaug, T. Inexact newton methods. *SIAM Journal on Numerical analysis*, 19(2):400–408, 1982.
- Deng, J., Dong, W., Socher, R., Li, L.-J., Li, K., and Fei-Fei, L. Imagenet: A large-scale hierarchical image database. In *2009 IEEE conference on computer vision and pattern recognition*, pp. 248–255. Ieee, 2009.
- Dhariwal, P. and Nichol, A. Diffusion models beat gans on image synthesis. *Advances in neural information processing systems*, 34:8780–8794, 2021.
- Efron, B. Tweedie’s formula and selection bias. *Journal of the American Statistical Association*, 106(496):1602–1614, 2011.
- Gatys, L. A., Ecker, A. S., and Bethge, M. Image style transfer using convolutional neural networks. In *Proceedings of the IEEE conference on computer vision and pattern recognition*, pp. 2414–2423, 2016.
- He, Y., Murata, N., Lai, C.-H., Takida, Y., Uesaka, T., Kim, D., Liao, W.-H., Mitsufuji, Y., Kolter, J. Z., Salakhutdinov, R., and Ermon, S. Manifold preserving guided diffusion. In *The Twelfth International Conference on Learning Representations*, 2024. URL <https://openreview.net/forum?id=o3Bx0Loxml>.
- Heusel, M., Ramsauer, H., Unterthiner, T., Nessler, B., and Hochreiter, S. Gans trained by a two time-scale update rule converge to a local nash equilibrium. *Advances in neural information processing systems*, 30, 2017.
- Ho, J. and Salimans, T. Classifier-free diffusion guidance. *arXiv preprint arXiv:2207.12598*, 2022.
- Ho, J., Jain, A., and Abbeel, P. Denoising diffusion probabilistic models. *Advances in neural information processing systems*, 33:6840–6851, 2020.
- Karras, T., Laine, S., and Aila, T. A style-based generator architecture for generative adversarial networks. In *Proceedings of the IEEE/CVF conference on computer vision and pattern recognition*, pp. 4401–4410, 2019.
- Kynkäänniemi, T., Karras, T., Aittala, M., Aila, T., and Lehtinen, J. The role of imagenet classes in fr chet inception distance. In *The Eleventh International Conference on Learning Representations*, 2023.
- Nichol, A. Q., Dhariwal, P., Ramesh, A., Shyam, P., Mishkin, P., McGrew, B., Sutskever, I., and Chen, M. Glide: Towards photorealistic image generation and editing with text-guided diffusion models. In *International Conference on Machine Learning*, pp. 16784–16804. PMLR, 2022.
- Podell, D., English, Z., Lacey, K., Blattmann, A., Dockhorn, T., M ller, J., Penna, J., and Rombach, R. SDXL: Improving latent diffusion models for high-resolution image synthesis. In *The Twelfth International Conference on Learning Representations*, 2024. URL <https://openreview.net/forum?id=di52zR8xgf>.
- Radford, A., Kim, J. W., Hallacy, C., Ramesh, A., Goh, G., Agarwal, S., Sastry, G., Askell, A., Mishkin, P., Clark, J., et al. Learning transferable visual models from natural language supervision. In *International conference on machine learning*, pp. 8748–8763. PMLR, 2021.
- Ramesh, A., Dhariwal, P., Nichol, A., Chu, C., and Chen, M. Hierarchical text-conditional image generation with clip latents. *arXiv preprint arXiv:2204.06125*, 1(2):3, 2022.

- Rombach, R., Blattmann, A., Lorenz, D., Esser, P., and Ommer, B. High-resolution image synthesis with latent diffusion models. In *Proceedings of the IEEE/CVF conference on computer vision and pattern recognition*, pp. 10684–10695, 2022.
- Rout, L., Raoof, N., Daras, G., Caramanis, C., Dimakis, A., and Shakkottai, S. Solving linear inverse problems provably via posterior sampling with latent diffusion models. In *Thirty-seventh Conference on Neural Information Processing Systems*, 2023. URL <https://openreview.net/forum?id=XKBFdYwfRo>.
- Saharia, C., Chan, W., Chang, H., Lee, C., Ho, J., Salimans, T., Fleet, D., and Norouzi, M. Palette: Image-to-image diffusion models. In *ACM SIGGRAPH 2022 conference proceedings*, pp. 1–10, 2022a.
- Saharia, C., Chan, W., Saxena, S., Li, L., Whang, J., Denton, E. L., Ghasemipour, K., Gontijo Lopes, R., Karagol Ayan, B., Salimans, T., et al. Photorealistic text-to-image diffusion models with deep language understanding. *Advances in neural information processing systems*, 35: 36479–36494, 2022b.
- Schuhmann, C., Beaumont, R., Vencu, R., Gordon, C., Wightman, R., Cherti, M., Coombes, T., Katta, A., Mullis, C., Wortsman, M., et al. Laion-5b: An open large-scale dataset for training next generation image-text models. *Advances in Neural Information Processing Systems*, 35: 25278–25294, 2022.
- Sohl-Dickstein, J., Weiss, E., Maheswaranathan, N., and Ganguli, S. Deep unsupervised learning using nonequilibrium thermodynamics. In *International conference on machine learning*, pp. 2256–2265. PMLR, 2015.
- Song, J., Meng, C., and Ermon, S. Denoising diffusion implicit models. In *International Conference on Learning Representations*, 2020.
- Song, Y., Sohl-Dickstein, J., Kingma, D. P., Kumar, A., Ermon, S., and Poole, B. Score-based generative modeling through stochastic differential equations. In *International Conference on Learning Representations*, 2021. URL <https://openreview.net/forum?id=PXTIG12RRHS>.
- Tan, W. R., Chan, C. S., Aguirre, H., and Tanaka, K. Improved artgan for conditional synthesis of natural image and artwork. *IEEE Transactions on Image Processing*, 28(1):394–409, 2019. doi: 10.1109/TIP.2018.2866698. URL <https://doi.org/10.1109/TIP.2018.2866698>.
- Tang, L., Jia, M., Wang, Q., Phoo, C. P., and Hariharan, B. Emergent correspondence from image diffusion. *Advances in Neural Information Processing Systems*, 36: 1363–1389, 2023.
- Yu, J., Xu, Y., Koh, J. Y., Luong, T., Baid, G., Wang, Z., Vasudevan, V., Ku, A., Yang, Y., Ayan, B. K., et al. Scaling autoregressive models for content-rich text-to-image generation. *arXiv preprint arXiv:2206.10789*, 2(3):5, 2022.
- Yu, J., Wang, Y., Zhao, C., Ghanem, B., and Zhang, J. Freedom: Training-free energy-guided conditional diffusion model. In *Proceedings of the IEEE/CVF International Conference on Computer Vision*, pp. 23174–23184, 2023.
- Zhang, L., Rao, A., and Agrawala, M. Adding conditional control to text-to-image diffusion models. In *Proceedings of the IEEE/CVF International Conference on Computer Vision*, pp. 3836–3847, 2023.
- Zhang, R., Isola, P., Efros, A. A., Shechtman, E., and Wang, O. The unreasonable effectiveness of deep features as a perceptual metric. In *CVPR*, 2018.

A. Analysis of the proposed algorithm

A.1. Convergence

We resort to *inexact Newton methods* (Dembo et al., 1982) to analyze the convergence and validity of the proposed approach. The original Newton’s method aims to solve the system

$$\mathbf{J}\mathbf{e}_t = \mathbf{e}. \quad (16)$$

In cases where computing the inverse of the Jacobian, as is the case of the diffusion denoiser Jacobian, inexact Newton methods propose first finding an approximation \mathbf{e}_t^* to the solution of Eq (16) and then performing the Newton step using the approximate solution and reiterating until convergence. For inexact Newton methods to converge to the correct solution, the residual must be strictly reduced at every step

$$\mathbf{r} = \mathbf{e} - \mathbf{J}\mathbf{e}_t^*, \quad \frac{\|\mathbf{r}\|_2}{\|\mathbf{e}\|_2} < \eta, \quad \eta \in [0, 1). \quad (17)$$

If we substitute the proposed update $\mathbf{e}_t^* = \lambda \mathbf{J}\mathbf{e}$ (Eq. 10) we get the residual

$$\mathbf{r} = \mathbf{e} - \lambda \mathbf{J}^2 \mathbf{e} = (\mathbf{I} - \lambda \mathbf{J}^2) \mathbf{e}. \quad (18)$$

For this residual to be strictly reduced at every iteration of our algorithm, we need

$$\frac{\|\mathbf{r}\|_2}{\|\mathbf{e}\|_2} = \frac{\|(\mathbf{I} - \lambda \mathbf{J}^2) \mathbf{e}\|_2}{\|\mathbf{e}\|_2} \leq \frac{\|\mathbf{I} - \lambda \mathbf{J}^2\|_2 \|\mathbf{e}\|_2}{\|\mathbf{e}\|_2} = \|\mathbf{I} - \lambda \mathbf{J}^2\|_2 < \eta. \quad (19)$$

Therefore, we need to show that the spectral norm of the matrix $\mathbf{I} - \lambda \mathbf{J}^2$ is smaller than 1 for a correct choice of learning rate λ .

If \mathbf{J} was diagonalizable (or more generally normal) then we could directly estimate $\|\mathbf{I} - \lambda \mathbf{J}^2\|_2$ using the largest eigenvalue of \mathbf{J} , following the spectral theorem. While we cannot directly assume that \mathbf{J} is normal, we know that \mathbf{J} should be ‘almost’ symmetric, as is the optimal denoiser solution shown in Eq. 14. This means that we could express $\mathbf{J} = \mathbf{S} + \mathbf{K}$, where $\mathbf{S} = (\mathbf{J} + \mathbf{J}^T)/2$ is the symmetric component and $\mathbf{K} = (\mathbf{J} - \mathbf{J}^T)/2$ the skew-symmetric component, and expect $\|\mathbf{K}\| \ll \|\mathbf{S}\|$. In that case, we can approximate $\|\mathbf{I} - \lambda \mathbf{J}^2\|_2$ as

$$\|\mathbf{I} - \lambda \mathbf{J}^2\|_2 \approx |1 - \lambda \max_i \mu_i^2| \quad (20)$$

where μ_i are the eigenvalues of \mathbf{S} .

To get an estimate of the magnitudes of the largest eigenvalues of \mathbf{S} , which are real, and of the eigenvalues of \mathbf{K} , which are imaginary, we use the Arnoldi iteration (Arnoldi, 1951). For the Arnoldi iteration we only require access to the matrix-vector products $\mathbf{J}\mathbf{v}$ and $\mathbf{J}^T \mathbf{v}$, which can be computed using the approximation of Eq. (12) and backpropagation respectively.

Running the Arnoldi iteration algorithm on \mathbf{J} , $(\mathbf{J} + \mathbf{J}^T)/2$ and $(\mathbf{J} - \mathbf{J}^T)/2$ we plot the magnitude of the largest eigenvalue of each matrix in Fig. 7 (a). We see that the contribution of the symmetric part of the matrix is the strongest, validating our assumption that the diffusion model’s Jacobian \mathbf{J} is ‘almost’ symmetric.

If we approximate the spectral norm of Eq. (19) using the symmetric component of the Jacobian we see that for a correct choice of λ we can ensure that $|1 - \lambda \max_i \mu_i^2| < 1$. Now we revisit the example of Fig. 1 where we inpaint half of the image. Instead of using the empirical learning rate used in the paper (linearly decreasing and gradient normalized by the ∞ -norm) we compute the largest eigenvalue of $(\mathbf{J} + \mathbf{J}^T)/2$, μ , and select different λ so that we satisfy or violate the bound provided by Eq. (20).

In Fig. 7 (b) we show that the error is not reduced for learning rate values that consistently violate the proposed bound. As expected, our algorithm consistently reduces the error at every iteration for a small enough learning rate, where the bound is always satisfied. When we use the empirical learning rate, shown in Fig. 7 (c), we see that the algorithm bounces between satisfying and not satisfying the computed bound and ends up at a lower error than the constant learning rate of Fig. 7 (b). We posit that the normalization by the ∞ -norm helps the learning rate adjust the step size such that it substantially reduces the error while not leading to divergence.

A.2. Difference between J and J^T

In the main text, we referred to the difference between J and J^T as a motivating factor for our approach and measured that difference by comparing elements (i, j) and (j, i) of the Jacobian matrix (Figure 2). In Figure 8 we further visualize the difference between using the Jacobian and its transpose by numerically computing how the Jacobian and the Jacobian transpose of the entire image would look for a single pixel, i.e. which parts of the image are affected by a change in a single pixel.

In Figure 8 we simplify the notation and denote as $J^{(i)}$ the Jacobian for a pixel i , which we compute by summing the squares of the matrix columns that correspond to this pixel’s latent values. If our approach were equivalent to backpropagation, i.e. $J = J^T$, then a change in a single pixel would have a similar effect on the rest of the image, up to some noise because of the finite difference approximation.

Contrary to the expectations, we find a significant difference between our proposed direction and backpropagation, with our approach having a better effect on retaining shapes and symmetry across the image. We see that in many cases, the model is trying to change ‘corresponding’ parts of the image together, i.e. change both eyes or ears simultaneously, giving us a better understanding of the knowledge that the model has acquired regarding the image space in general.

B. Proposed algorithm as modification of DDIM

To apply the proposed method we modified the DDIM sampling algorithm (Song et al., 2020). We provide a side-by-side comparison to show the difference between the original DDIM and the proposed algorithm. Extending our algorithm to other sampling methods should be intuitive by alternating between gradient updates from our algorithm and the diffusion updates computed with the diffusion sampling algorithm used.

Algorithm 2 DDIM sampling (Song et al., 2020) using a pre-trained diffusion model.

- 1: **Input:** Pre-trained diffusion model $\hat{x}_0(x_t)$, diffusion step size s and schedule parameters α_i, β_i
 - 2: $x_T \sim N(\mathbf{0}, I)$
 - 3: **for** $t \in \{T, T-s, T-2s, \dots, s\}$ **do**
 - 4: $z_t \sim N(\mathbf{0}, I)$
 - 5: $\epsilon_t = \frac{1}{\sqrt{1-\alpha_{t-s}}}x_t - \frac{\sqrt{\alpha_{t-s}}}{\sqrt{1-\alpha_{t-s}}}\hat{x}_0(x_t)$
 - 6: $x_{t-s} = \sqrt{\alpha_{t-s}}\hat{x}_0(x_t) + \sqrt{1-\alpha_{t-s}}\epsilon_t + \beta_{t-s}z_t$
 - 7: **end for**
 - 8: **Return:** x_0
-

Algorithm 3 The proposed algorithm for constrained sampling using a pre-trained diffusion model.

- 1: **Input:** Pre-trained diffusion model $\hat{x}_0(x_t)$, **constraint** $C(x_0, y) = \|f(\hat{x}_0(x_t)) - y\|_2^2$, **condition** y , **gradient step size** δ , **iterations** K , **learning rate** λ , diffusion step size s and schedule parameters α_i, β_i
 - 2: $x_T \sim N(\mathbf{0}, I)$
 - 3: **for** $t \in \{T, T-s, T-2s, \dots, s\}$ **do**
 - 4: **for** $i \in \{1, 2, \dots, K\}$ **do**
 - 5: $e = J_f^{-1}(f(\hat{x}_0(x_t)) - y)$ {Task-dependent}
 - 6: $e_t = [\hat{x}_0(x_t + \delta e) - \hat{x}_0(x_t)]/\delta$
 - 7: $x_t = x_t + \lambda e_t$
 - 8: **end for**
 - 9: $z_t \sim N(\mathbf{0}, I)$
 - 10: $\epsilon_t = \frac{1}{\sqrt{1-\alpha_{t-s}}}x_t - \frac{\sqrt{\alpha_{t-s}}}{\sqrt{1-\alpha_{t-s}}}\hat{x}_0(x_t)$
 - 11: $x_{t-s} = \sqrt{\alpha_{t-s}}\hat{x}_0(x_t) + \sqrt{1-\alpha_{t-s}}\epsilon_t + \beta_{t-s}z_t$
 - 12: **end for**
 - 13: **Return:** x_0
-

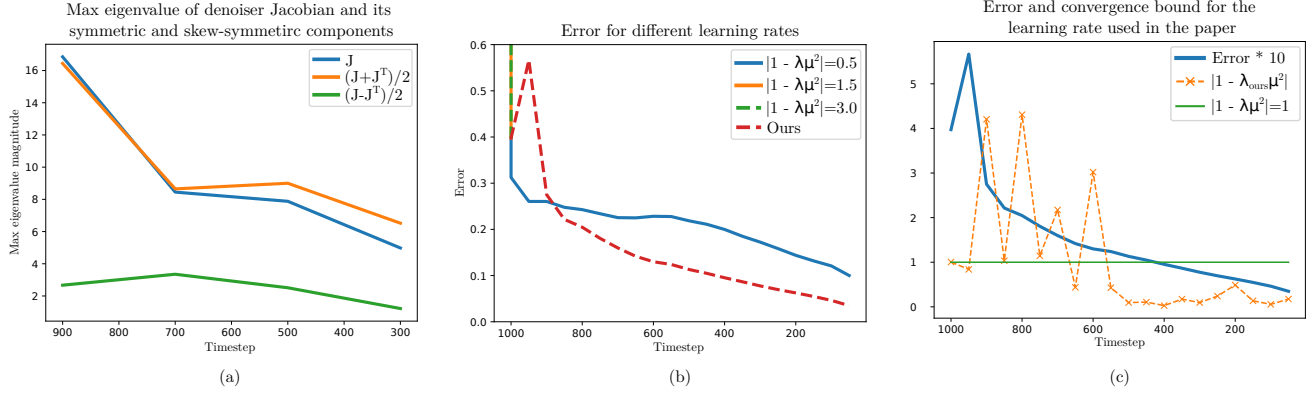


Figure 7. Using the proposed analysis we visualize in (a) the largest eigenvalue of J as well as its symmetric and skew-symmetric components. The largest eigenvalue follows closely the largest eigenvalue of the symmetric part of the matrix. In (b) we demonstrate the convergence of our method for different learning rates. In (c) we show that our adaptive learning rate scheme initially oscillates around the theoretical convergence bound and eventually settles well-below it. These initial oscillations may be important for the high-quality results, as using lower learning rate did not attain similar-quality images.

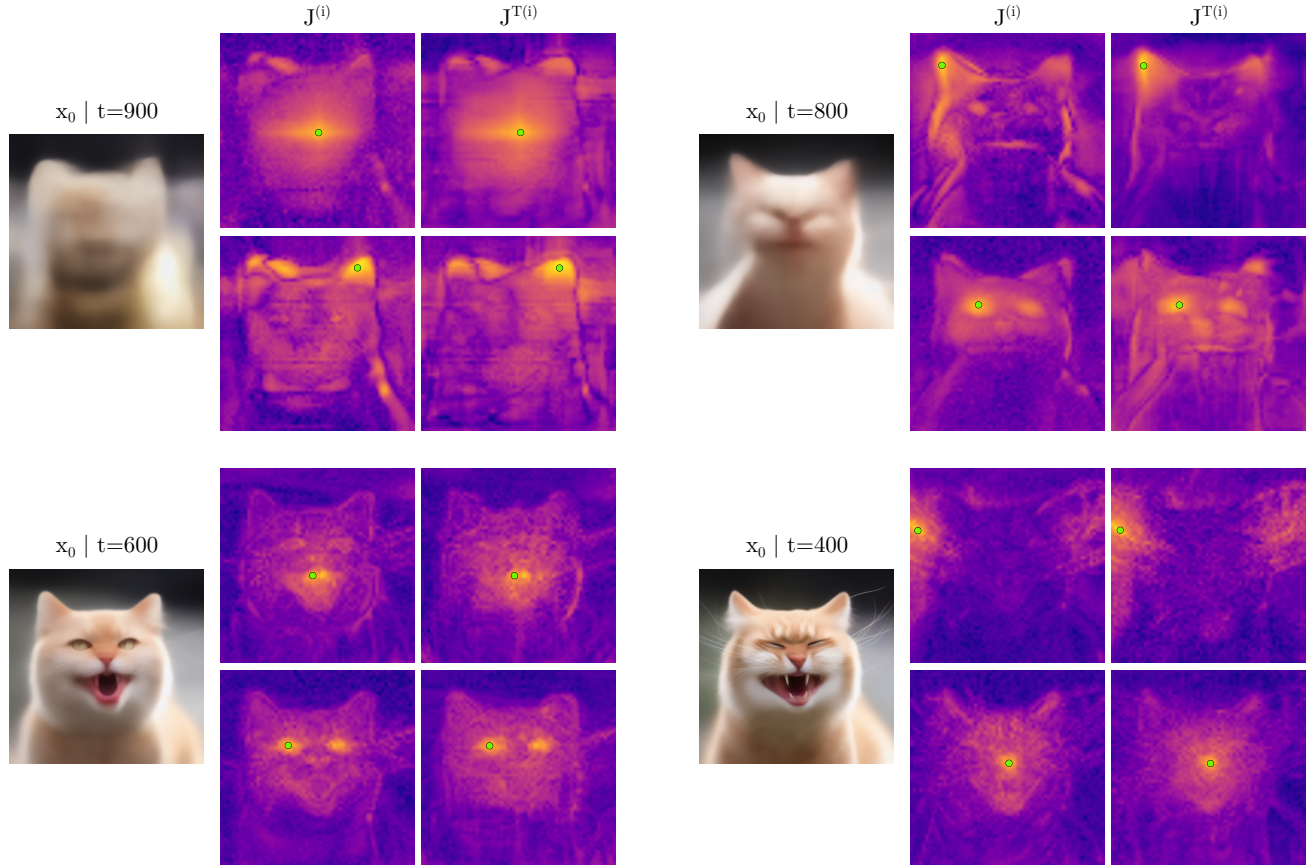


Figure 8. We visualize the difference between J and J^T by computing how the matrix wants to change the entire image would look for a perturbation of a single pixel. By $J^{(i)}$ we denote this exact change, which corresponds to the sum of 4 columns in the matrix (4 latent channels per-pixel). Our proposed update direction better captures longer-range dependencies by better maintaining shapes. Even though we use a numerical approximation, the proposed direction is sharper in regions, like the outline of the cat.

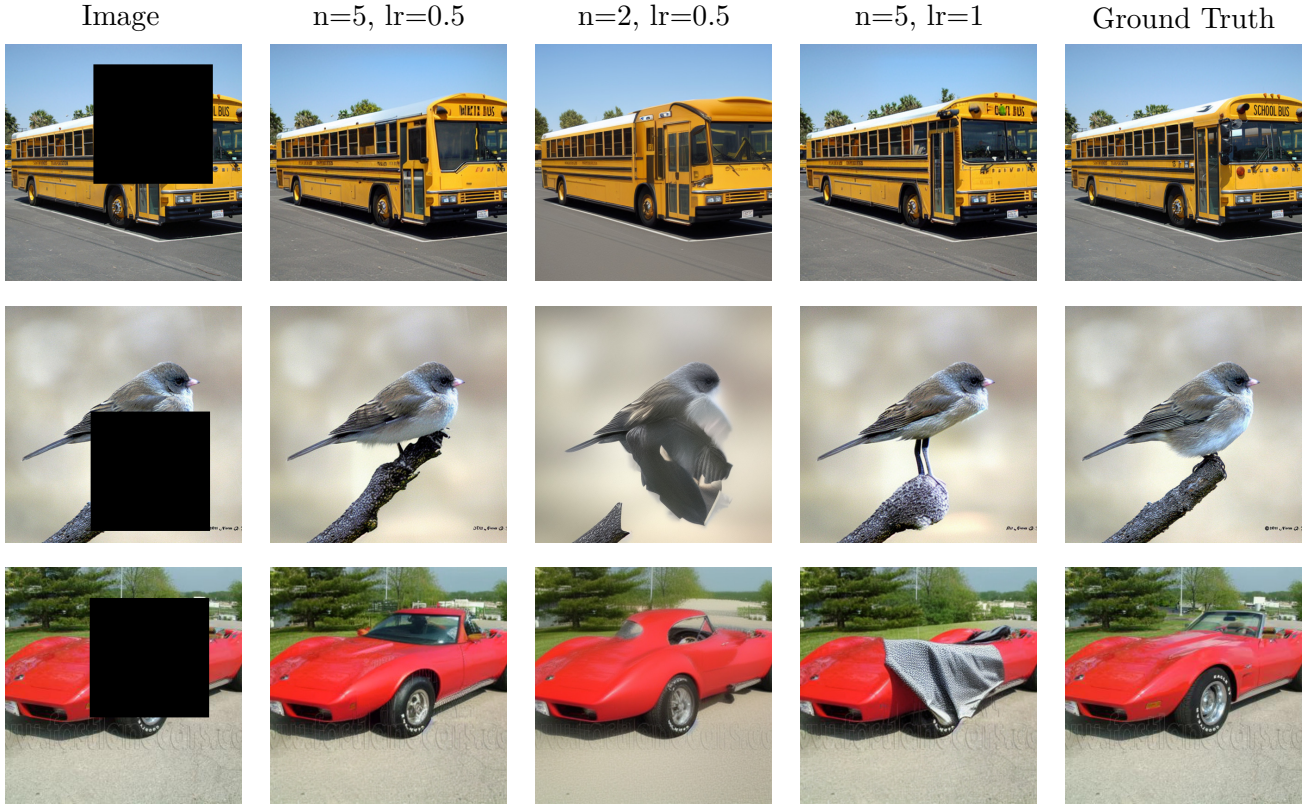


Figure 9. Examples of box inpainting when using different optimization steps and learning rates.

C. Additional Results

C.1. Number of steps and learning rate ablation

We repeat the ImageNet box inpainting experiments with fewer optimization iterations and a higher learning rate. We show qualitative results in Figure 9, where we observe that running fewer optimization steps gives blurrier results, which is expected as the known regions of the image also seem to not have converged to the given values. Using a higher learning rate leads to the model sometimes ‘overshooting’ by inpainting the missing regions with realistic-looking parts that do not necessarily fit the rest of the image. The quantitative results are presented in Table 5.

Method	PSNR \uparrow	LPIPS \downarrow	FID \downarrow
Ours (n=5, lr=0.5)	18.30	0.30	42.01
Ours (n=2, lr=0.5)	18.01	0.39	68.75
Ours (n=5, lr=1.0)	17.48	0.32	47.20

Table 5. Ablation of the number of steps and learning rate on box inpainting. When using fewer steps, the algorithm does not sufficiently converge. When using a very high learning rate, the approach seems to overshoot to non-realistic inpainted parts.

C.2. Non-differentiable constraints

There is no restriction on defining the constraint C as long as we can get the direction e towards which we want to push the image x_0 . In the non-linear constraint case, we resorted to using the gradient descent direction $J_f^T(f(x_0(x_t)) - y)$ to avoid computing the inverse Jacobian of f . In theory, any direction e that locally minimizes the constraint can be used with the proposed algorithm.

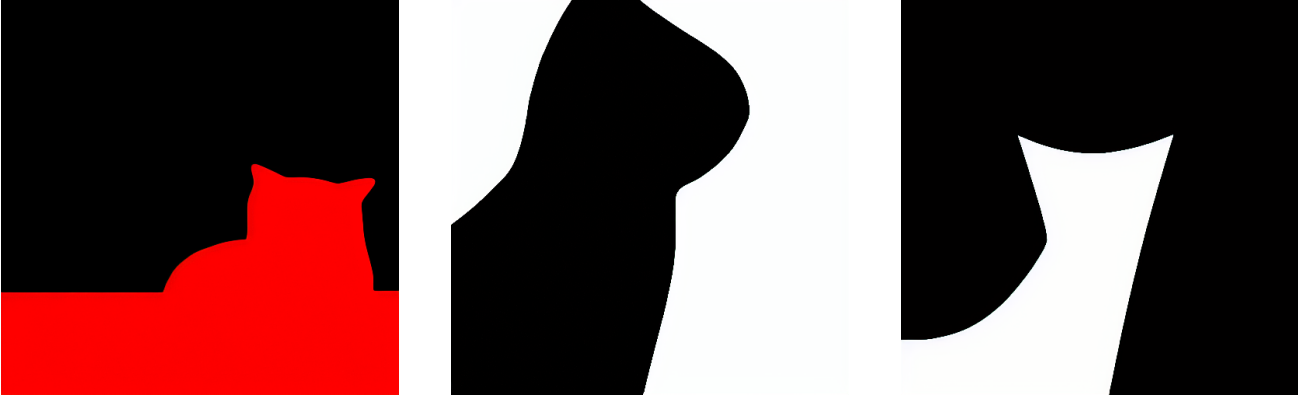


Figure 10. We apply a non-differentiable constraint to generate quantized images. Using the prompt ‘a photo of a cat’ we generated binary images of cats.

As a toy example, we generate images with pixel values quantized to be either ‘on’ or ‘off’ (-1 or 1). The constraint first measures whether a pixel value is positive or negative and then sets the error direction e to $|1 - x|$ or $|-1 - x|$ for every pixel accordingly. This is a non-differentiable constraint for which we can easily compute a local gradient that reduces the cost C . Using the prompt ‘a photo of a cat’, we generate quantized images as shown in Figure 10.

C.3. Inference visualizations

In Figures 11, 12, and 13, we visualize the intermediate steps of the proposed algorithm for the inpainting, super-resolution and style-guided generation tasks respectively. Our method quickly converges to a plausible image and then further refines it to better satisfy the constraint over the diffusion timesteps. For style-guided generation, we see that the structure of the image is defined in the first few initial steps before the specific style provided is applied.

C.4. Effect of convergence speed on final images

We ask the question of *how does convergence speed affect the quality of the generated images?* Previous works found that applying a high weight on the constraint led to unwanted artifacts in the generated images (Chung et al., 2023). We hypothesize that, apart from artifacts in the gradient, ‘over-optimizing’ for the condition at a given timestep can affect the generation quality. In practice, if we push the initial x_t too far from the inputs the denoiser network is expecting, either with a high weight on the gradient update or by performing too many updates, we should be seeing non-realistic images in the output.

We investigate this by running the same inpainting experiment with 5 optimization steps per timestep (Figure 14) and 20 optimization steps (Figure 15). Although we expected to see a difference in the final generated images, we find that both converge to similar quality results. Our proposed optimization steps at a single timestep consider the Jacobian of the denoiser model, which we find acts as ‘regularization’ and makes it difficult to produce x_t inputs that satisfy the condition ‘early’. Even when running the optimization for more steps at a single x_t , we see that although the sample converges faster to the desired condition, the denoiser is still able to continue the diffusion process of x_t .

C.5. More Qualitative Results

In Figure 4 we provided qualitative results on free-form inpainting and super-resolution. In inpainting, our model consistently performs as well as the slowest baseline, P2L. For super-resolution, P2L which also infers a prompt seems to generate better-fitting textures for the images. We hypothesize that by also inferring a prompt the high-frequency detail generation is better-guided in the super-resolution task. In contrast, in inpainting, the non-masked pixels contain enough information about the textures that need to be placed around the image.

In Figure 16 we showcase additional results on the box inpainting task. MPGD (He et al., 2024), which does not backpropagate the constraint error through the diffusion model completely fails at inpainting the missing region. We attribute

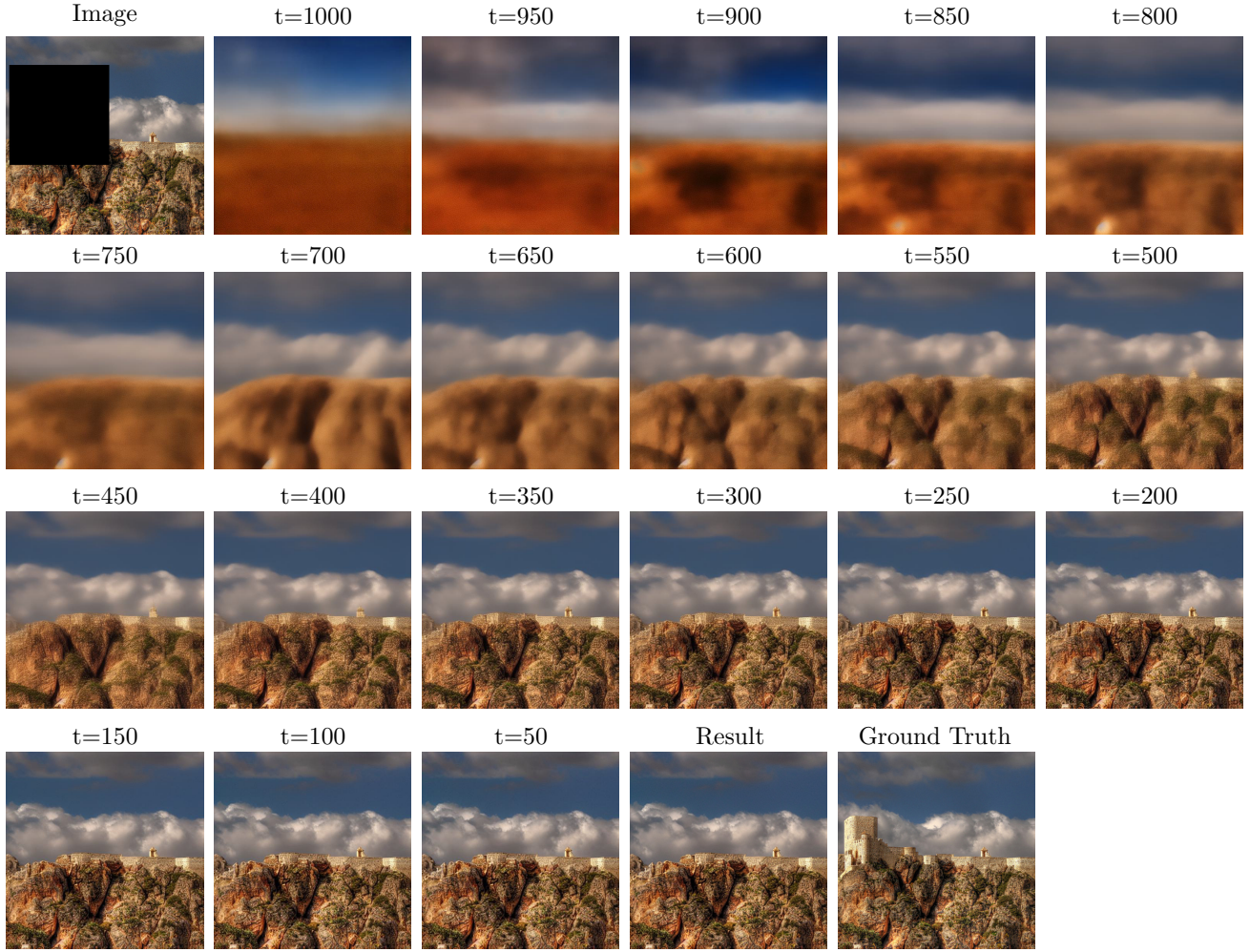


Figure 11. Visualization of the intermediate inference steps for the inpainting task.

that to the minimal ability to influence pixels that are ‘far’ from the constraint at lower noise levels without probing the model weights. The *Naive* algorithm replaces the known pixels in the estimated final image at every denoising iteration.

In Figure 17 we present additional results on style-guided text-to-image generation for a single prompt. Qualitatively, we see that the style of the images generated with our algorithm better matches the style of the reference image, even when using a different model to define style (OpenCLIP). In Figure 18 we show images generated with different styles and text prompts. Here, we show how increasing the classifier-free guidance weight w (Ho & Salimans, 2022) controls the influence of the text prompt on the final generated image.

In Figure 19 we provide qualitative results of our segmentation mask-guided generation experiment. We see that the baseline of MPGD either over-satisfies the constraint by burning in artifacts ($\rho = 1$) or fails to generate images that adhere to the constraint ($\rho = 0.5$). Our approach generates the most realistic images while also getting the mask prediction to match to the reference image. Since we are using Stable Diffusion, we used the text prompt ‘a headshot photo’ to constrain the set of possible generated images. As expected, the results are not on par with an FFHQ-specific model, but we still find our algorithm able to synthesize good images even in this difficult case.

In Figure 20 we include more samples from the experiment in Section 3.2 in the main paper. We observe that the proposed gradient updates regularly give more consistent outputs that repeat textures across the image. We attribute this to the difference between \mathbf{J} and \mathbf{J}^T we discussed in A.2.

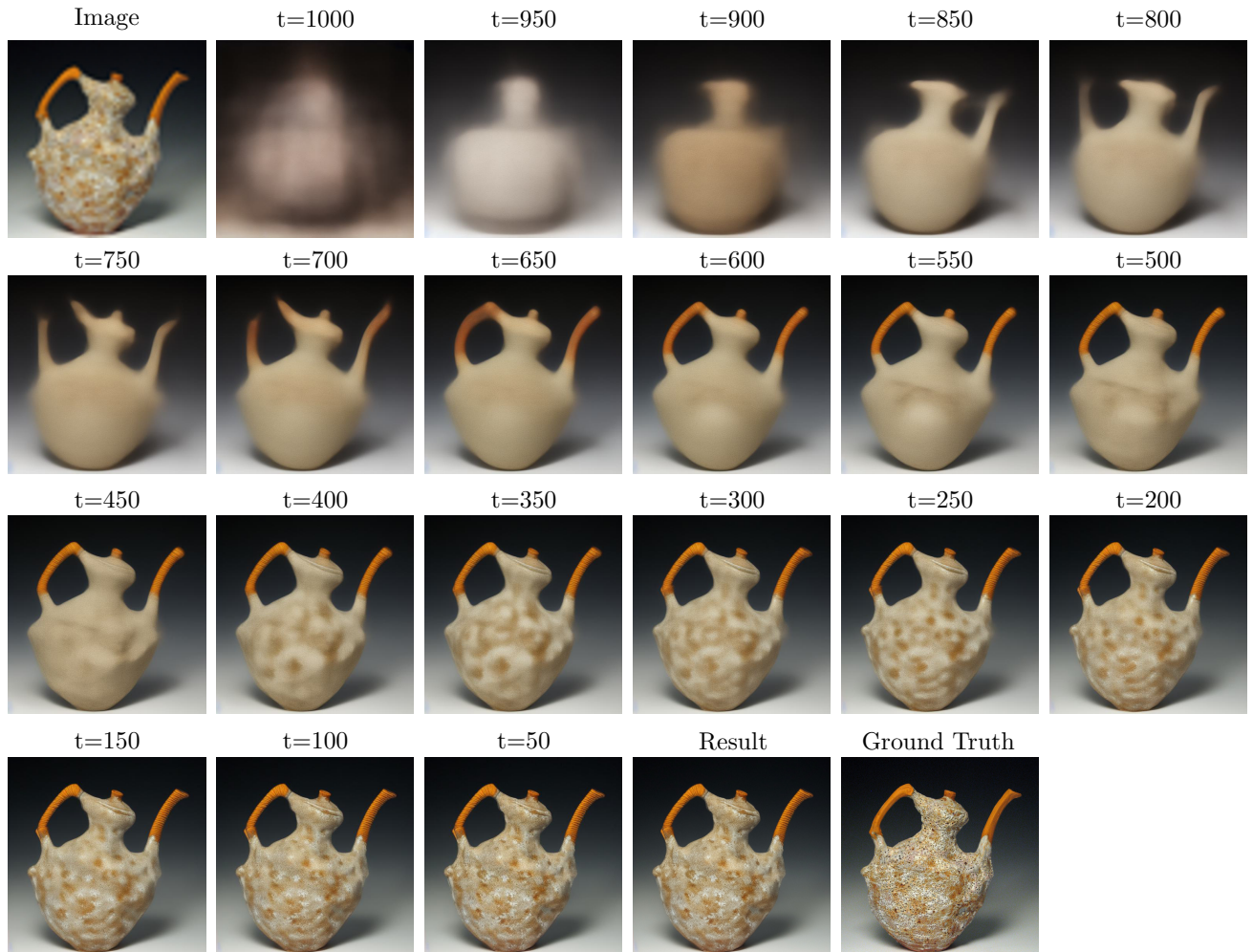


Figure 12. Visualization of the intermediate inference steps for the super-resolution task.

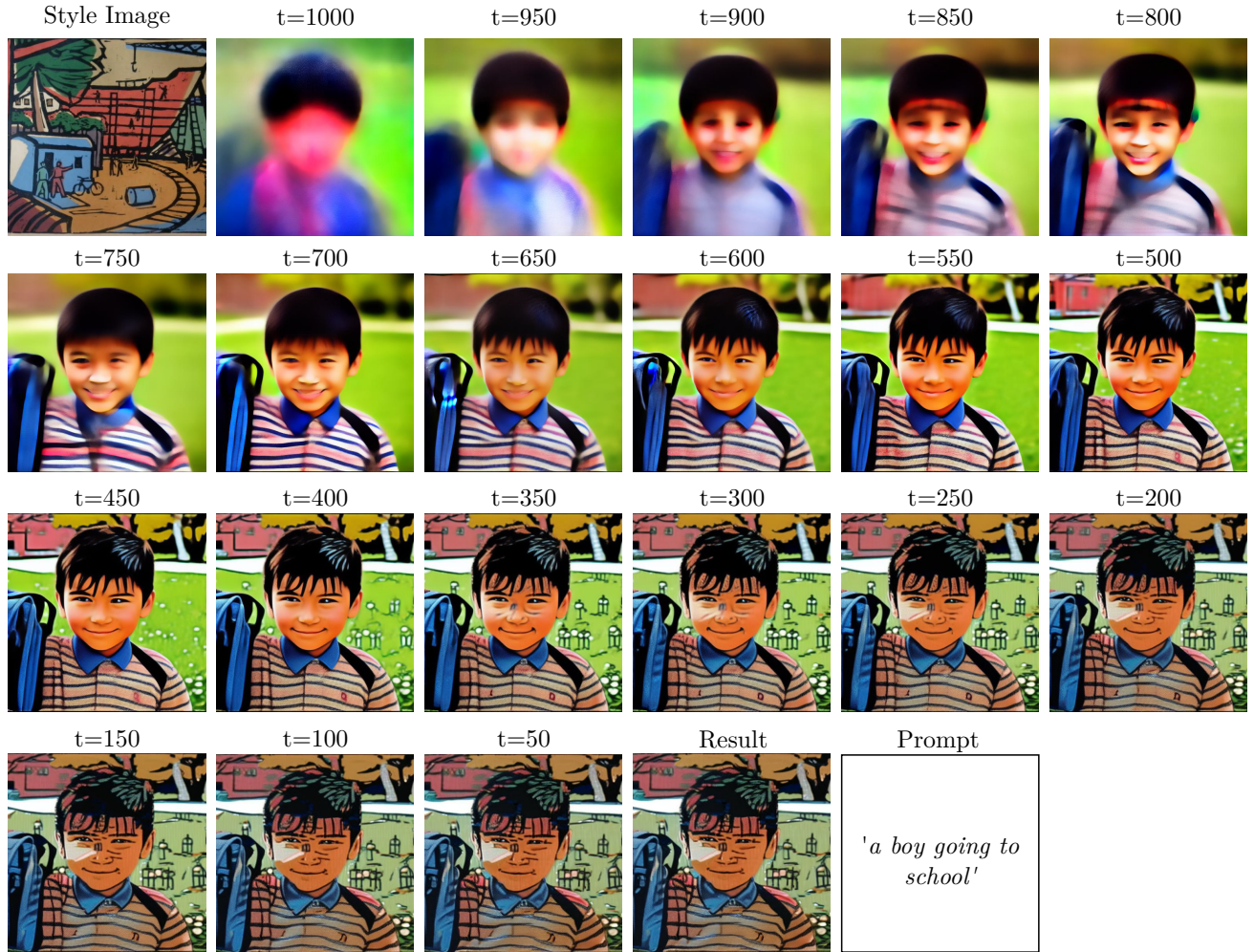


Figure 13. Visualization of the intermediate inference steps for the style-guided generation task.

5 steps

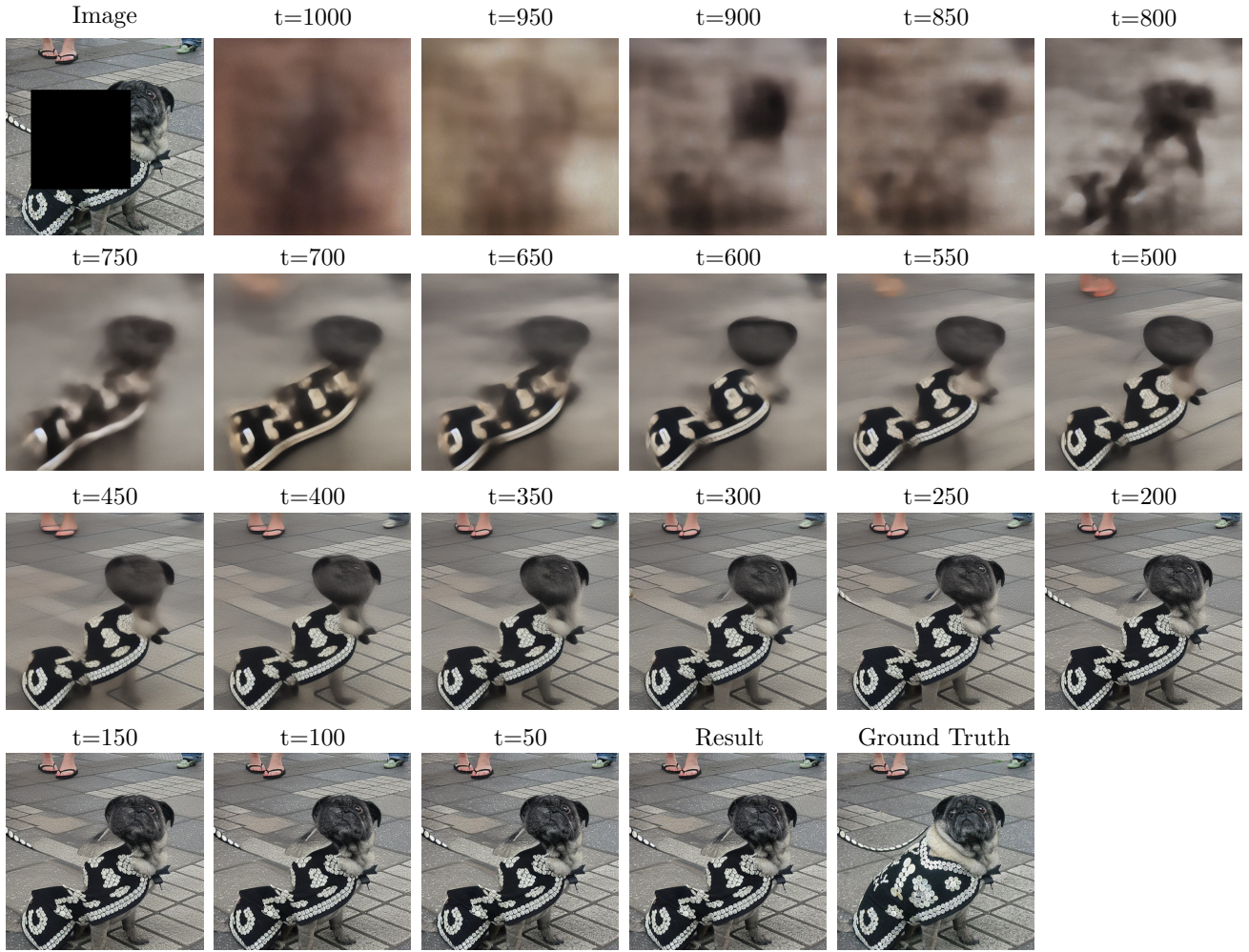


Figure 14. Convergence for the inpainting task when using 5 optimization steps K .

20 steps

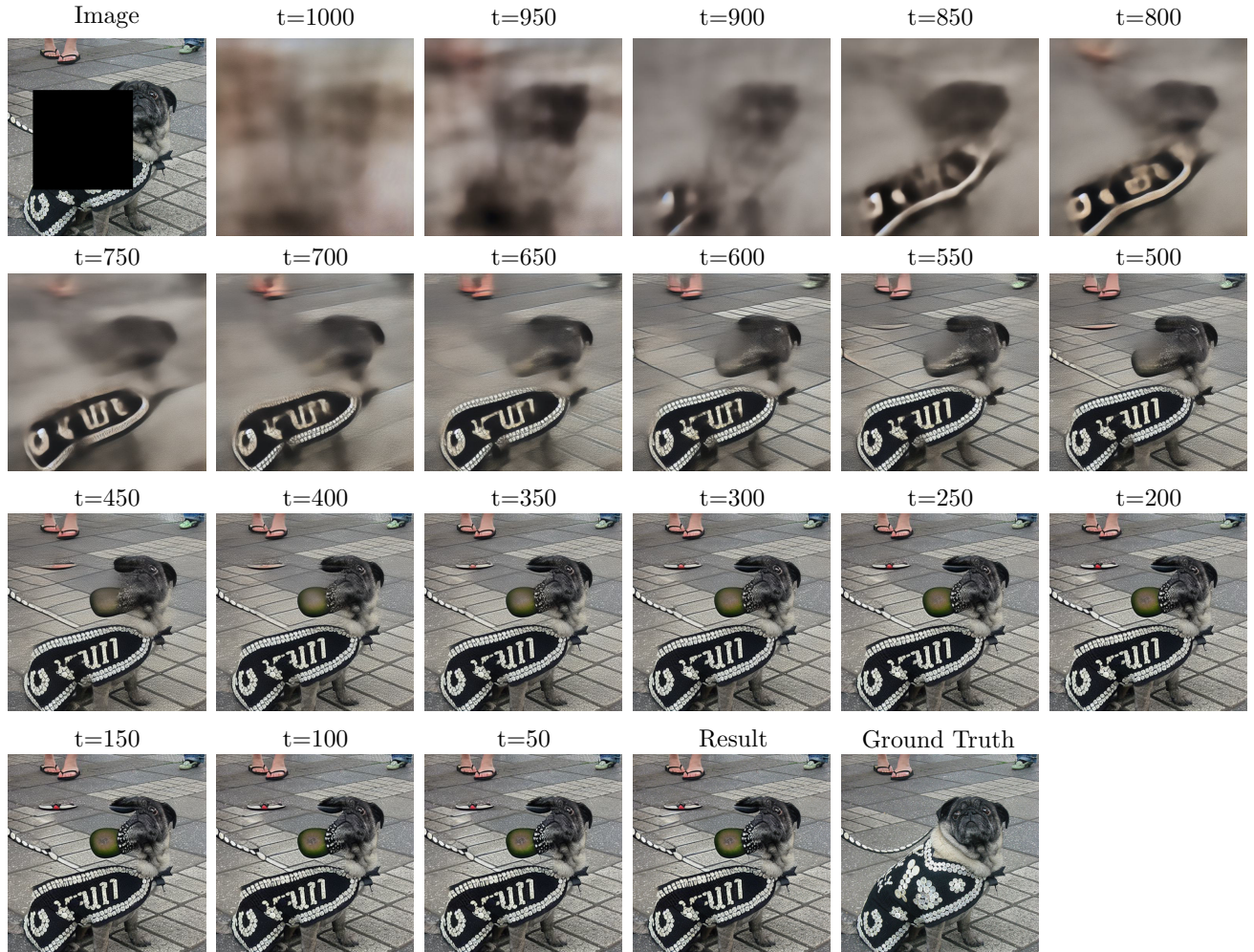
Figure 15. Convergence for the inpainting task when using 20 optimization steps K .



Figure 16. Box inpainting examples for all methods. Naive replaces the pixels with their true values + noise during inference.

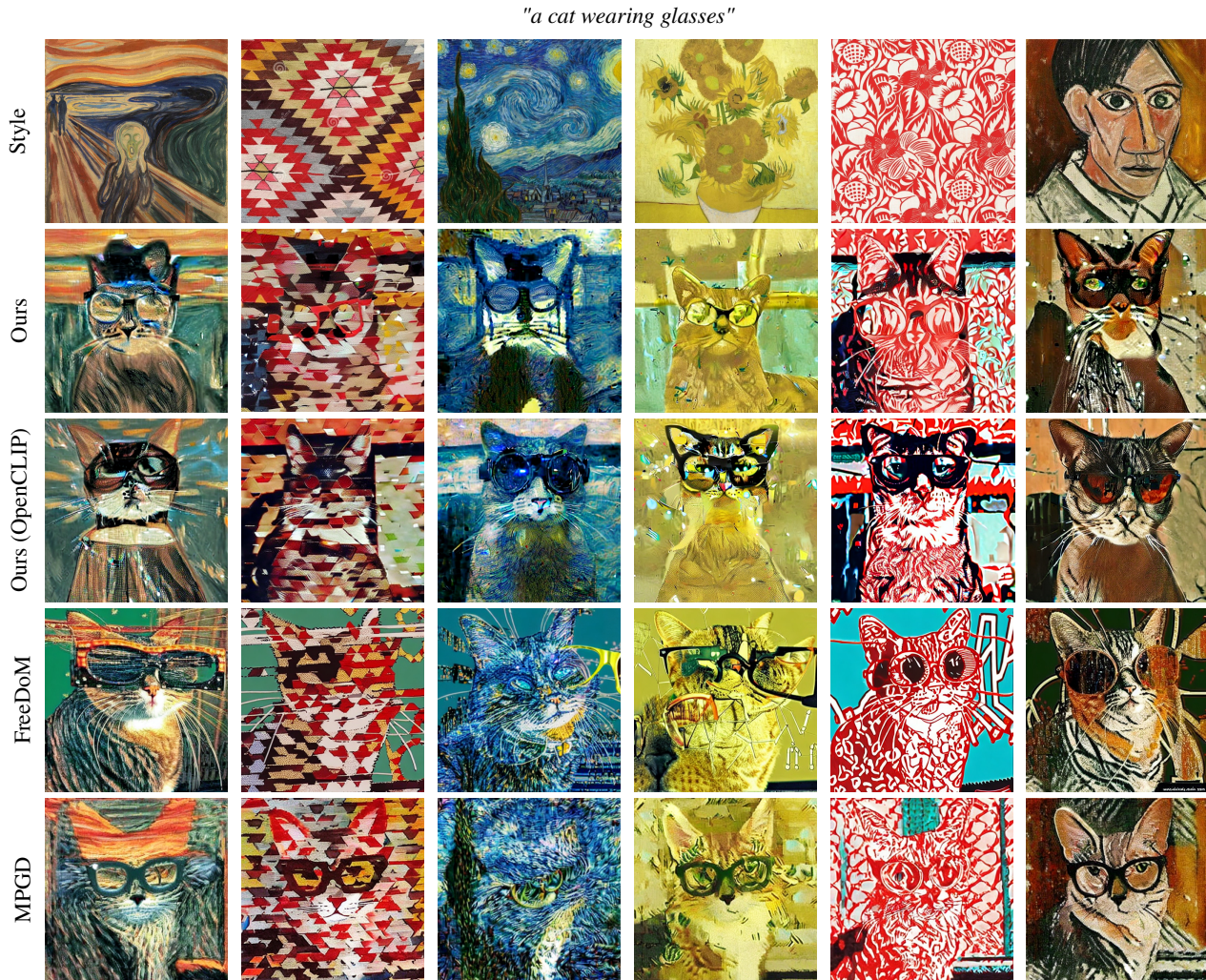


Figure 17. Examples of style-guided text-to-image generation for a single prompt and multiple styles.



Figure 18. Examples of style-guided text-to-image generation for multiple prompts and styles.

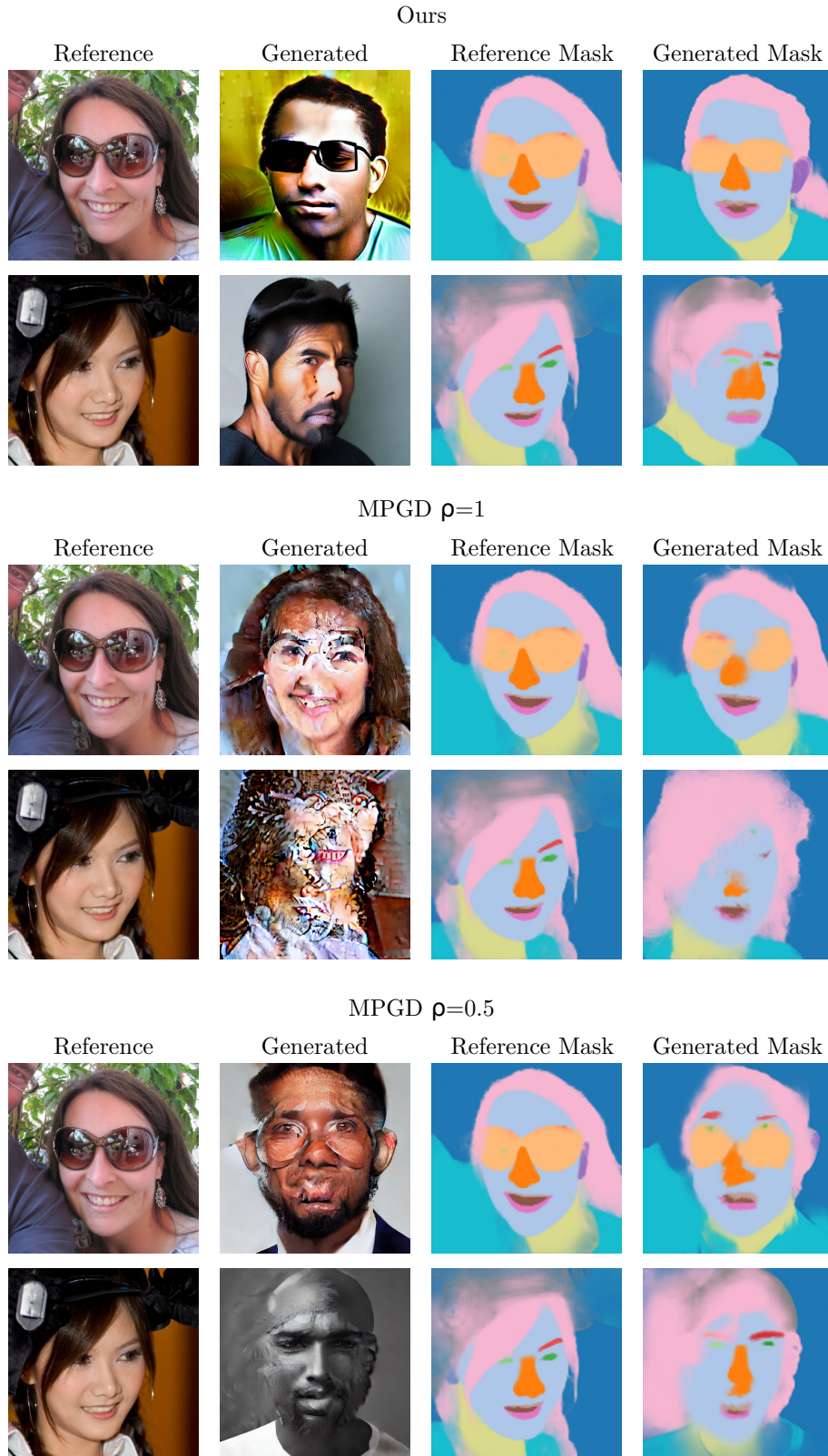


Figure 19. Examples of segmentation-guided generation using our method and MPGD.

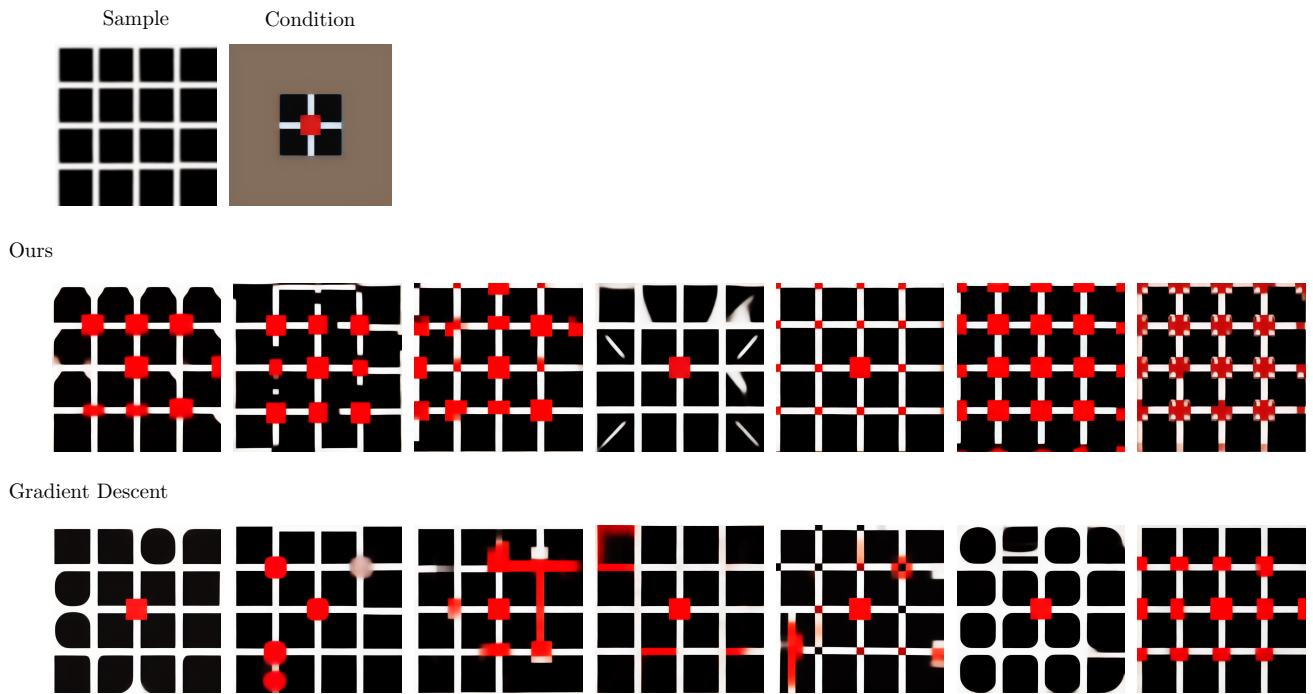


Figure 20. Comparison between gradient descent and the proposed gradient. The setup is the same one as in Section 3.2.